

Theranostics of Epitaxially Condensed Colloidal Nanocrystal Clusters, through a Soft Biomimetic Route

Giorgio Zoppellaro,[†] Argiris Kolokithas-Ntoukas,[‡] Katerina Polakova,[†] Jiri Tucek,[†] Radek Zboril,[†] George Loudos,[#] Eirini Fragogeorgi,^{#,△} Clemens Diwoky,[⊥] Katerina Tomankova,[○] Konstantinos Avgoustakis,[§] Dimitris Kouzoudis,^{||} and Aristides Bakandritsos*,[‡]

[†]Regional Centre of Advanced Technologies and Materials, Department of Physical Chemistry, Palacky University, 783 71 Olomouc, Czech Republic

[‡]Department of Materials Science, [§]Pharmacy Department, ^{||}Department of Chemical Engineering, University of Patras, 26504 Rio Patras, Greece

[#]Department of Biomedical Engineering, Technological Educational Institute, GR 122 10 Athens, Greece

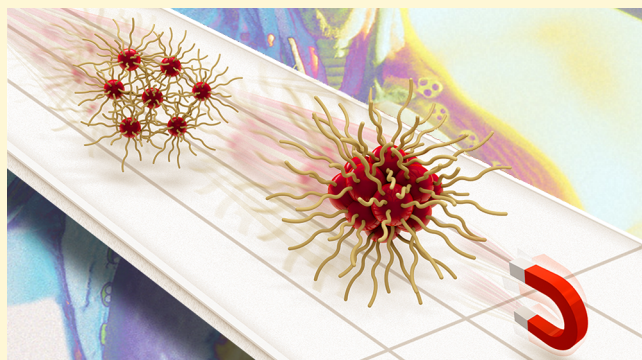
[△]Institute of Radioisotopes-Radiodiagnostic Products, N.C.S.R. 'Demokritos', GR 153 10 A Paraskevi, Greece

[⊥]Graz University of Technology, Institute of Medical Engineering, A-8010 Graz, Austria

[○]Department of Medical Biophysics, Faculty of Medicine and Dentistry, Institute of Translation Medicine, Palacky University, 775 15 Olomouc, Czech Republic

Supporting Information

ABSTRACT: Clustering of biocompatible magnetic iron oxide nanocrystallites (MIONs) is a synthetic strategy which improves magnetic manipulation, imaging, and sensing for biomedical applications. In this work we describe the synthesis of condensed clustered MIONs obtained through biomimetic and epitaxial aggregation in the presence of alginate at ambient conditions, mimicking the process that so far has been achieved only by nature, in iron-oxidizing bacteria. These condensed-type magnetic nanostructures exhibit higher magnetophoretic responses compared to other types of magnetic colloids and clustered systems. The soft environmental conditions used for the synthesis of the magnetic nanosystems enables the alginate coating material to retain high drug loading ability for the doxorubicin molecule as well as strong binding proclivity for radionuclides. The strong binding of doxorubicin forms the physical basis to obtain magnetic nanocarriers, where the selective release of the drug occurs only under the action of external stimuli, such as remote magnetic hyperthermia or increased temperature (i.e., inflamed tissue). Furthermore, the strong binding proclivity of radionuclides facilitates *in vivo* SPECT imaging. The witnessed properties are obtained by using only ~17 wt % alginate content in the magnetic superstructures; thus, very high saturation magnetization value is imparted to the condensed system, expressed in terms of the hybrid's mass. In spite of the fact that the magnetic nanoassemblies are characterized by low hydrodynamic diameter, ~45 nm, the transverse relaxivity reaches the remarkable value of $250 \text{ s}^{-1} \text{ mM}^{-1} \text{ Fe}$ (for negative MION contrast agents of this size), a property that validates the use of these nanostructures as effective MRI contrast agents.



INTRODUCTION

Colloidal nanoassemblies of magnetic iron oxide nanocrystallites (MIONs) have attracted considerable research interest, in part due to their expected high impact on the field of theranostics^{1–11} and other biomedical applications such as sensing^{7–11} and separations.^{12,13} Owing to the continued focus on such colloids and better understanding of structure–property relationships, new advances in the field have shed light on the synthetic pathways toward colloidal nanocrystal clusters (CNCs).^{7–56} CNCs refer to superstructures of nanocrystallites organized into higher order colloidal entities (Figure 1a,b).

Generally, MION-based CNCs have been grown either by one-step direct solution growth^{14–29,31,33,35} or by two step synthetic paths, utilizing preformed MIONs. In the latter case, clustering can be achieved through solvophobic interactions^{36–53} in micelles,^{37–43} polymersomes^{45–47} and liposomes,^{48–52} for example. Growth of CNCs has been also realized by compartmentalization in^{54–56} or decoration of nanosilica.³⁰

Received: December 10, 2013

Revised: February 12, 2014

Published: February 17, 2014

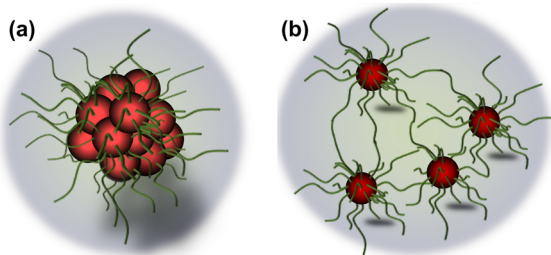


Figure 1. Schematic drawing of the (a) condensed colloidal nanocrystal cluster (epitaxial aggregation) and (b) soft colloidal nanocrystal cluster (bridging motif).

Nanochains or nanoworms represent other forms of nanoparticle's clustering, with particular shape-driven advantages in imaging and targeting.^{21,57–59} More detailed summary of the synthetic methodologies pursued by various groups in the field can be found in recent reviews.^{60,61} From the structural perspective and considering all MION-based CNCs systems assembled to date, a particularly interesting architecture refers to CNCs of densely packed MIONs in such a fashion that their crystal planes adopt the same orientation through epitaxial aggregation. In this scenario the crystallites of ~50–300 nm size show single-crystal-like structure throughout large areas of their volume and yet behave like ensembles of smaller independent (5–15 nm) nanocrystallites. Hence, they exhibit superparamagnetism and large broadening of the XRD envelopes (i.e., the respective of the 5–15 nm size).^{16,18,22,25,28} The first, almost simultaneous, reports on MION nanostructures encoding such structural organization were published by Zhu et al.¹⁵ and Ge et al.¹⁶ in 2007, works that soon inspired other groups that used similar synthetic procedures.^{17–20,22,25,26} Nevertheless, as early as 2005, Deng et al.¹⁴ synthesized already CNCs, but it was not mentioned in the report that what appeared as "single-crystals" was the result of the oriented/epitaxial attachment of MIONs. Later, Luo et al. upon following the same synthetic procedure were able to validate such property.²² In reference to this particular type of structural organization, we will use throughout the text the term condensed-CNCs (co-CNCs, Figure 1a) in order to distinguish this type of nanostructure from other CNCs (soft-CNCs) where MIONs are not assembled through oriented aggregation or direct attachment. In the latter case, MIONs are embedded in other matrices (micelles, silica, liposomes, etc.) or are clustered together through polymers in bridging configuration^{29–35} (Figure 1b).

CNCs feature high technological potential in the medical domain of theranostics.^{7,8,17,19,20,23–25,34,62–65} The first advantage that these systems hold compared to conventional magnetic nanosystems arises from their high magnetic moment and the consequent higher force exerted by external magnetic fields during magnetic separation^{16,31,49} or within manipulation/targeting applications.^{29,31,35,64} The second advantage is related to their superior contrast ability for clinical imaging (MRI), as indexed by the high transverse relaxivity values obtained upon clustering.^{7,8,21,25,27,30,32,34,37,39,44,45,53,54,57} It is quite indicative that such characteristic has been used as a sensitive tool for the detection of biomolecular interactions.^{7,8} It has been also predicted that condensed clustering may increase transverse relaxation by 2-fold.⁸ Another benefit arising from the use of co-CNCs architecture is their ability to cage a higher number of MIONs, that is better magnetic properties, in comparison to

soft-CNCs, considering constant hydrodynamic diameter. All these factors reinforce the idea that co-CNCs have the potential to produce a superior functional response for *in vivo* theranostic applications.

From the chemist's perspective the synthesis of co-CNCs has been a challenge for long time. In the early stage of research, co-CNCs were synthesized from FeCl_3 , sodium acetate, and ethylene glycol under solvothermal conditions at high temperature ($200\text{ }^\circ\text{C}$) and for 8 h of reaction, a process that led to the assembly of 200 nm cluster diameter.¹⁴ Advances in the synthesis of co-CNCs were published only years later by using similar starting materials and reaction temperature ($220\text{ }^\circ\text{C}$), but following a friendlier route, under normal pressure.¹⁶ Furthermore, in the same work, the presence of poly(acrylic acid) as organic shell provided colloidal stability for the magnetic nanoparticles in distilled water. Similar synthesis was employed by other groups by replacing poly(acrylic acid) with citric acid,^{19,66} poly(glutamic acid),²³ or carboxymethylcellulose²⁴ as well as other biopolymers.⁶² One recent report demonstrated that the use of microwave radiation for the synthesis of co-CNCs under high pressure can be used as an alternative method to shorten the otherwise long reaction times required for their assembly.²⁶ On the basis of the recent reviews^{60,61} and the references cited throughout, according to which all MIO-based co-CNCs are grown under thermolytic or solvothermal conditions, it is evident that a significant improvement in the field would benefit greatly from the development of synthetic pathways toward co-CNCs prepared at ambient conditions.

This work reports the attainment of such a straightforward synthetic route for the first time. The preparation of MIO-based co-CNCs at $50\text{ }^\circ\text{C}$ and at ambient pressure in the presence of a biopolymer is showcased, a process that so far has been attained only in nature, by iron-oxidizing bacteria toward iron oxyhydroxide phases.⁶⁷ In the lab-bench, the co-CNCs synthesis is realized through a soft biomineralization route of magnetite, through arrested alkaline precipitation of Fe^{II} only ions, in the presence of sodium alginate. This is also the first time that a remarkable difference in magnetic manipulation between condensed- and soft-CNCs is described, after selection of appropriate CNC samples, which were subjected to magnetophoretic studies. The present co-CNCs form an excellent substrate for theranostic applications, as evidenced by the results obtained from drug loading and triggered release, cytocompatibility, magnetophoresis, MRI, and SPECT imaging.

■ EXPERIMENTAL SECTION

Materials. $\text{FeSO}_4 \times 7\text{H}_2\text{O}$ (Lab NV), sodium alginate (Sigma-Aldrich, viscosity of 2% solution at $25\text{ }^\circ\text{C}$: ~250 cps), HCl (Carlo Erba), NaCl (Merck Chemicals), NaOH (Merck Chemicals), NH_4OH (30%) Carlo Erba, and Doxorubicin (EBEWE Pharma Ges.m.b.H). Technetium-99m was used as a $\text{Na}^{99\text{m}}\text{TcO}_4$ solution in saline, eluted from a commercial Mallinckrodt Medical B.V. ^{99}Mo – $^{99\text{m}}\text{Tc}$ generator. Biodistribution studies were performed using female normal Swiss mice (15–25 g) of the same colony and age, purchased from the Breeding Facilities of NCSR "Demokritos". All other chemicals were supplied from Sigma-Aldrich.

Synthesis. The 300 mg of alginate was dissolved in H_2O (60 mL). NH_3 (4 mL, 30%) was added to the polymer solution. Then 1440 mg of $\text{FeSO}_4 \times 7\text{H}_2\text{O}$ (in 20 mL of H_2O containing 60 μL of 37% HCl) was added. The mixture was heated at $50\text{ }^\circ\text{C}$ under magnetic stirring and the reaction stopped after 1 h and 30 min. The product was purified from byproducts and fractionated following the same protocol as previously described for MagP(MAA-g-EGMA)1 (or MagP as

shortly coded throughout this article).³⁵ A sample with primary magnetic crystallite size of 6 nm was prepared following the coprecipitation route, which used FeCl₃ in addition to FeSO₄ × 7H₂O in a 2:1 molar ratio.

Protocols for colloidal stability, Fe concentration (expressed as Fe₂O₃ % w/v) measurements, doxorubicin determination, drug loading, and release experiments have been previously described in detail.³⁵

DLS, XRD, TGA, and TEM Characterization. Dynamic light scattering (DLS) was performed on aqueous dispersions of ~0.01% w/v in Fe₂O₃. Electrokinetic measurements for the determination of the mobility and zeta-potential (ζ_p) values of the suspensions were performed with a Malvern Instrument ZetaSizer Nano and with a 4 mW He–Ne laser, operating at a wavelength of 633 nm. DLS was performed using the same instrument, where scattered light was collected at a fixed angle of 173°. The hydrodynamic diameters (D_h) reported are the mean of three measurements, and each measurement was the sum of 12 correlograms and fitting procedures. The cumulants analysis was applied, and the D_h average values reported are the z-average mean D_h , unless otherwise stated. The reported polydispersity index (PDI) values, ranging between 0 for an ideally monodispersed sample and 1 for a system with very broad size distribution, have been derived from the formula PDI = σ^2/D_h^2 , where σ is the standard deviation of the distribution in nanometers.

X-ray diffraction (XRD) was performed on a D-800 Siemens diffractometer, with Ni-filtered Cu K α radiation. Samples were dried on a glass plate and then collected and ground and finally spread with the aid of ethanol on the Bruker sample holder with a Si wafer for low sample volumes.

The polymer content in the hybrid materials was determined with thermogravimetric measurements (TA Instruments, Q500). Measurements were performed under N₂ flow.

Samples for TEM were prepared by casting a droplet of a dilute aqueous suspension (0.01% w/v in Fe₂O₃) of the hybrids on copper grids coated by Formvar carbon film. Micrographs were obtained by a JEOL, JEM-2100 instrument operating at 200 kV.

SQUID Magnetization Measurements and ⁵⁷Fe Mössbauer Spectroscopy. A superconducting quantum interference device (SQUID, MPMS XL-7, Quantum Design) has been used for the magnetic measurements.

The transmission ⁵⁷Fe Mössbauer spectra were measured using a Mössbauer spectrometer in a constant acceleration mode with a ⁵⁷Co(Rh) source. The isomer shift values were related to α-Fe at room temperature. The measurements were carried out employing a closed-helium cycle device at the temperatures of 300 and 150 K without the application of an external magnetic field. The acquired Mössbauer spectra were fitted with the MossWinn software package; prior to fitting, the signal-to-noise ratio was enhanced by a statistically based algorithm developed by Prochazka et al.⁶⁸

Magnetophoresis. The magnetophoretic experiments were performed using a Hitachi Digilab U-2800 spectrophotometer and by inserting next to the cuvette holder a cylindrical Nd–Fe–B magnet (diameter = 20 mm, thickness = 10 mm) at a distance of 2 mm, as previously described.²⁸ The concentration of all the magnetic colloids in all experiments was set at 0.012% w(Fe₂O₃)/v.

Hyperthermia. Hyperthermia experiments were performed on 1% w(Fe₂O₃)/v dispersions of MagAlg on a custom-made apparatus (Supporting Information Figure S1) at a field of 50 Oe (4 kA m⁻¹) and at 400 kHz. For the drug release experiment the AC field was applied for 10 min. The instrument was built from KEL, S. Roudis, Greece. In another setup used only for capturing infrared images, a system obtained from Five Celes that consists of a generator, a coil, and a cooling system was used. MagAlg nanocarriers were dispersed in double-distilled water, sealed in a 2 mL microcentrifuge vial, and placed inside the coil. Temperature increase was continuously monitored using an infrared camera (FLIR E30).

Computational Studies. The screening of the conformational space in the simplified MagAlg-Dox system (namely, a model containing two alginate chains composed by alternating L-guluronate (G) and D-mannuronate (M) residues (6-mer each chain) placed in

close proximity to each other including one doxorubicin molecule) was performed by using a combination of the Merck Molecular Mechanics Force Field (MMFF94aq)/Monte Carlo methods, followed by geometry optimization of the best scored conformer using the semiempirical Recife Model 1 (RHF/RM1) method. The heat-of-formation was calculated at -15291.70 kJ/mol. The number of basis functions used for this system was 869, and the molecular charge of MagAlg-Dox system was set to zero and spin multiplicity set to 1. Calculations were carried out using the computational package Spartan 14 (parallel version 1.0.0, Wave function Inc., Irvine, CA, U.S.A.).

In Vitro Tests. Cytotoxicity of the prepared nanoparticles was evaluated on MCF7 cells (Caucasian breast adenocarcinoma) using the MTT assay. Cells were incubated with MagAlg of various concentrations (5.73–0.0596 mg/mL) in 96 well plates (P-Lab, Czech Republic) at 37 °C and 5% CO₂ for 24 h. Before starting the MTT experiments DMEM (Dulbecco's modified Eagle's medium with 10% fetal bovine serum) was replaced by PBS (phosphate buffered saline, pH = 7.4), containing 5 mM glucose, then we added 10 μL of 20 mM MTT (3-(4,5-dimethyl-2-thiazolyl)-2,5-diphenyl-2H-tetrazolium bromide) dissolved in PBS and incubated the cells for 3 h at 37 °C and 5% CO₂. The MTT solution was carefully removed, and we added 100 μL of DMSO in order to solubilize the violet formazan crystals. The absorbance of the resulting solution was measured in a 96-well microplate reader Synergy HT (BioTek, U.S.A.) at 570 nm. The cell viability of the samples was determined as the percentage of control cell viability (100 × average of test group/average of control group).

The same MTT test was used for the determination and comparison of cytotoxicity effect of free doxorubicin and MagAlg loaded with doxorubicin. The appropriate amount of preloaded MagAlg was used in order to perform studies with the same drug concentration (50.0, 5.0, and 0.5 μM of doxorubicin). The IC₅₀ value was statistically determined by 3T3NRU Phototox software (COLIPA, Germany).

Magnetic Resonance Imaging and Relaxometry. Measurements were performed with a clinical 3T whole-body MR scanner (Siemens Skyra, Erlangen, Germany). For all measurements a circular polarized animal coil with an inner diameter of 7.5 cm (RAPID Biomedical GmbH, Rimpar, Germany) was used to gain high signal-to-noise ratio.

R_2 relaxometry measurements were realized with a 2D Carr–Purcell–Meiboom–Gill (CPMG) sequence with an echo-spacing of 11.1 ms and 24 echos, TR = 5000 ms, FOV = 90 × 73 mm, phase-oversampling (OS) = 50%, matrix = 192 × 156, and a single 5 mm slice. Additionally a T_2^* weighted image was taken with a 2D Gradient-Echo (GRE) sequence with TE = 12 ms, TR = 200 ms, alpha = 25°, NEX = 8, FOV = 120 × 71 mm, matrix = 120 × 71, and a slice thickness of 1.5 mm.

R_1 was measured employing an inversion-recovery–fast-spin-echo (IR-FSE) and six different inversion times (50, 100, 200, 400, 800, 1600, 3200 ms), at a temperature of 23.2°, a turbo-factor of 3, TR = 5000 ms, FOV = 90 × 73 mm, phase-OS = 50%, matrix = 192 × 156, and a single 5 mm slice.

Transverse and longitudinal relaxation times were calculated using a self-written program (IDL, Exelis Inc., CO, U.S.A.). T_2 was determined with a linear fit of the logarithmized signal intensity over echo time (for all used TEs the SNR was >5), whereas the first echo was ignored. T_1 was calculated using a three-parameter fit of the IR-FSE data set according to the signal equation: $S_{IR} = A (1 - B \exp(-T_1/T_1))$.

Finally, r_1 and r_2 were computed as the slope of the linear regression between R_1 and R_2 , and the Fe concentration is expressed in mM.

In Vitro Stability Studies of the Radiolabeled CNCs. The in vitro stability of the bond between MagAlg and the reduced Tc-99m was studied in fresh human serum, PBS (pH 7.4), as well as in the presence of cysteine solution. A blood sample from healthy donors in a plain serum gel tube (red-cherry cap) was clotted for at least 30 min at room temperature and centrifuged at 2200g at 4 °C for 10 min, and the supernatant (serum) was collected. One hundred microliters (7.4–11.1 MBq or 200–300 μCi) of each radiolabeled nanoparticle were incubated in fresh human plasma (900 μL), in PBS (100 μL), and in

Cysteine (100 μ L, 10 mM) at a water bath of 37 °C with constant shaking. Aliquots of 90 μ L were taken at 1, 3, and 5 h after mixing, and these were centrifuged at 15 000g for 20 min. The radioactivity of the pellets and supernatants of these aliquots was measured to provide the percentage of radioactivity bound to the nanoparticles.⁶⁹

Radioactivity was measured using a dose calibrator from Capintec, Inc. Instant thin layer chromatography (ITLC) was developed on ITLC-SG (Gelman Sciences), while the measurements were performed with an electronic autoradiography system (Instant Imager Packard-Canberra). Radioactivity of samples during biodistribution studies was measured by a multisample gamma-counter, a Packard Minaxi 5500 equipped with a 3 in. NaI (TI) crystal.

Biodistribution of Radiolabeled CNCs. In vivo studies were performed in compliance with the European legislation for animal welfare. All animal protocols have been approved by the Hellenic Authorities. The in vivo behavior was studied in normal female Swiss mice (average weight 20 ± 2.0 g) by injecting 100 μ L (2×10^{-3} % w/v, MBq or 70–120 μ Ci) of nanoparticle through the tail vein. Animals were sacrificed at predetermined time intervals of 60 and 120 min post injection (p.i.) and the main organs were removed, weighed, and counted, together with samples of blood, muscle, and urine, in a gamma-counter. In reference to a standard of the injected solution, results were expressed as a percentage of the injected dose (% ID) per organ and per gram of each organ or tissue. For total blood radioactivity calculation, blood is assumed to be 7% of the total body weight. Dynamic images of the injected mice were obtained from the 10–15th min postinjection (p.i.) up to 1 h p.i., and a static image was taken at 24 h p.i. Right after injection, animals were anaesthetized using a mixture of 0.5 mL of ketamine hydrochloride (100 mg/mL), 0.25 mL of xylazine (20 mg/mL), and 4.25 mL of NaCl 0.9%. The anesthesia dose for each animal was 0.1 mL/10 g of animal weight and was administered intraperitoneally. All animals were dropped to anesthesia approximately within 5–10 min p.i. and positioned to the animal bed for the scanning.

In Vivo Scintigraphic Imaging. Dynamic imaging was carried out using a high resolution gamma-camera with a 5 × 10 cm field of view and 1.5 mm spatial resolution. The system is based on (i) a parallel hole collimator, 25 mm thick, with hexagonal holes 1.1 mm in diameter and 0.25 mm septa; (ii) a 5 × 10 cm pixelized NaI scintillator, 5 mm thick, with 1 × 1 mm² pixels and 0.25 mm septa; and (iii) two square H8500 PSPMTs, each one 50 × 50 mm in size. Mice are placed anaesthetized in a short distance (<1 cm) from camera head and sequential, 2 min images, are stored. The 2 min images are summed to obtain an image of high statistics where regions of interest (ROIs) are drawn; then those ROIs are applied to the 2 min frames, to achieve semiquantitative time activity curves.

RESULTS AND DISCUSSION

We have previously reported the successful growth of soft-CNCs acting as nanocarriers for the drug doxorubicin (Dox). These systems were obtained from the arrested precipitation of a single ferrous precursor in the presence of either carboxymethyl cellulose⁷⁰ or a graft copolymer of PEG on poly(methacrylic acid) backbone (termed earlier as MagP-(MAA-g-EGMA)1³⁵ and coded briefly here as MagP) forming the polymeric corona. In the frame of our systematic research on the structural and biophysicochemical properties of magnetic nanoassemblies produced for theranostic applications, we report here and compare with previous results the structure and properties of the magnetic product obtained by using the biogenic and biodegradable polymer sodium alginate. Although alginate has been used by other groups as coating material for magnetic nanoparticles during⁷¹ or following⁷² coprecipitation of Fe²⁺ and Fe³⁺ ions, the experimental conditions employed by us led to emergence of unique structural and physicochemical characteristics in the magnetic nanoassemblies (MagAlg). At the end of the reaction, fractionation of the crude mixture was

performed by centrifugation, in order to isolate colloids having similar D_h to that previously obtained for the MagP system (~85 nm, z-average). In this way comparative results could be drawn, and, furthermore, the nanoassemblies produced displayed size that would not preclude long blood circulation.^{73,74}

The product MagAlg was examined by Mössbauer spectroscopy, and it was found to be composed of nonstoichiometric magnetite (see Supporting Information for analysis of the results and Figure S2). From now on and for clarity, the magnetic phase will be called magnetite throughout the text. The size of the nanocrystallites obtained from XRD analysis (Figure 2a, green squares) was determined at ~13 nm, hence

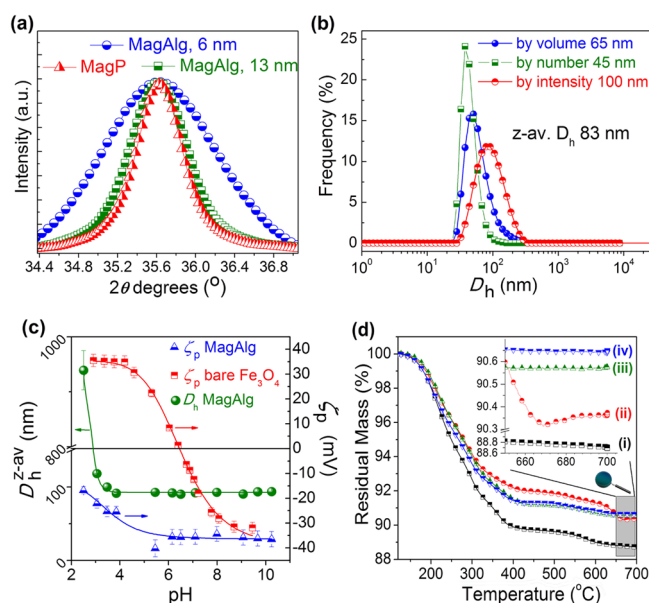


Figure 2. (a) XRD data of MagAlg (6 nm), MagAlg (13 nm), and MagP materials focused on the 311 reflection. (b) DLS of MagAlg, PDI = 0.16 ± 0.02 . (c) DLS and ζ_p measurements of MagAlg and uncoated magnetite vs pH. (d) TGA traces and selected area magnification (inset) of MagAlg (i) after one washing by magnetic separation and decantation of the reaction byproducts and (ii), (iii), and (iv) after two, three, and four successive washings by centrifugation and redispersion.

slightly lower than those observed for MagP (15 nm, Figure 2a, red triangles). Upon performing the reaction using the coprecipitation route, nanocrystallites with significantly smaller diameter were produced, with dimension of approximately 6 nm (Figure 2a, blue circles). In Figure 2b, the detailed results obtained for MagAlg from DLS analysis are collected together. Here, attention is paid on how D_h is expressed, since it profoundly affects the values if D_h is reported by number, by volume, intensity, or as z-average. The number-weighted D_h of MagAlg was determined as ~45 nm while the z-average D_h as ~83 nm. Thus, the hydrodynamic size of MagAlg was found nearly identical to that previously determined for MagP. The similar D_h 's for the two products is an important indicator in order to compare their magnetophoresis response, since we have previously shown that magnetophoretic velocity highly depends on the D_h (retaining all other parameters constant),³⁵ due to its connection to the viscous drag force (vide infra), but mainly due to the different masses of magnetic material associated with MION-colloids of different D_h .

Table 1. Inorganic Contents of the Studied Nanoassemblies As Derived from TGA and Magnetometry Results^a

sample	polymer content (% wt)	T (K)	$M_{s\pm}$ ((A m ²)/kg)	$M_s^{\text{Fe}_2\text{O}_3,b}$ ((A m ²)/kg)	B_C (mT)	M_R ((A m ²)/kg)
MagP	11 ± 3	5	83.5	83.5	17.0	22.4
		300	74.3		0	0
MagAlg	17 ± 3	5	82.6	85.6	9.3	19.6
		300	71.1		0	0

^a $M_{s\pm}$ is the saturation magnetization at ± 7 T, $M_s^{\text{Fe}_2\text{O}_3}$ is the saturation magnetization with respect to the magnetic material content only, B_C is the coercive field, and M_R is the remanent magnetization. ^bThese values were deduced after taking into consideration the polymer mass contents in the colloids, which were determined from TGA analysis (shown in Figure 2d for MagAlg and in ref 35 for MagP).

The effective surface functionalization of the MIONs with the alginate polyelectrolyte became evident from the very different ζ_p dependence on pH (Figure 2c, blue triangles) in comparison to uncoated MIONs (Figure 2c, red squares). The ζ_p trend of the latter (uncoated) has been previously reported,⁷⁵ but it is presented here for comparative reasons. The ζ_p of MagAlg remained highly negative and only at pH < 4 carboxylate groups started to become protonated, thus shifting ζ_p to less negative values. The stability of the system followed this trend, with the D_h remaining stable above pH = 4. On the contrary, uncoated MIONs displayed their isoelectric point at ~ 6.5 , the value at which they already started to flocculate.⁷⁵ It is worth mentioning that an important structural factor to consider pertains to the stability of the polymeric corona upon high dilution⁷⁶ (i.e., resistance on desorption), which is a scenario that the nanocarriers are going to experience upon application in biological environments. The knowledge of such a stability parameter is as important as the knowledge of the critical micelle concentration in the case of micellar type nanocarriers.^{77,78} Although it is clear that carboxylate groups interact with the surface metal ions of the MIONs (probed with FT-IR for example⁷⁰), this factor cannot provide a priori any solid evidence for the polymer's grafting strength. Therefore, Tóth et al.⁷⁶ performed measurements of the free polymer after dilution $\times 2$, in order to verify that no polymer was desorbed from the nanoparticle's surface. In the present case MagAlg was subjected to harsh tests by successive washings and redispersions in deionized H₂O (Figure 2d). Every washing and redispersion equals to 20 \times dilution, since after each centrifugation the pellet (100 μ L) was redispersed in a total of 2 mL of H₂O. Specifically, at the end of this first washing procedure, MagAlg was separated with a magnet and its mass loss was measured ($\sim 11\%$ mass loss, line (i) in Figure 2d inset). Then, a portion of the one-time washed product was subjected to the second washing and the witnessed mass loss was 9.65%. After three and four washings the mass losses were 9.45 and 9.35%, respectively (lines ii, iii, and iv, in Figure 2d, inset). Therefore, these mass changes in the last three washings are practically negligible and confirm the very strong interactions that alginate develops with the surface of the MIONs, even after extremely high dilution. It should be noted that the mass losses reported are not the polymer contents. The latter (as presented in Table 1) are derived after taking into consideration the residue of neat alginate after TGA (Figure S3 in the Supporting Information).

SQUID Analysis. The achievement of high saturation magnetization (M_s) in MION-based colloids has been a subject of high importance. The quest of obtaining superstructures combining high M_s while remaining functional (for instance small size and effective drug loading) is highlighted in the work of H. Xu et al.³⁶ (and references therein) where M_s of 40 A m² kg⁻¹ is considered as a very high M_s value. More recently,

Wang's team prepared co-CNCs as drug delivery agents²³ with M_s varying from 80.5 and 66.9 to 64.4 A m² kg⁻¹ for CNCs having 230, 220, and 150 nm diameter, respectively (estimated by TEM, thus D_h would be significantly larger). This range of sizes is prohibitive for applications necessary for long blood circulation,^{73,74} as mentioned by the authors in their follow up work, where they prepared drug-carrying co-CNCs of $D_{\text{TEM}} = 100$ nm.⁷⁹ Nevertheless, in this case the M_s dropped down to 27 A m² kg⁻¹ of hybrid, while D_h was determined as large as 350 nm. Finally, in another recent example,²¹ M_s of 62.4 A m² kg⁻¹ for polymer coated co-CNCs has been considered as an example of nanostructures with "remarkable magnetic response". These reports are indicative of the difficulty encountered so far in obtaining magnetic theranostic materials combining harmoniously all the critical properties for their effective application. In this context, we have illustrated here the aforementioned examples in order to underpin the relevance of our finding, that is, polymer-coated co-CNCs having particularly small size may as well display exceptional M_s , as discussed in the following.

Looking at the hysteresis loops recorded for MagP and MagAlg at 5 K, they clearly show the higher coercive field of the former (34.6 mT) compared to the latter (19.1 mT) (Figure 3b

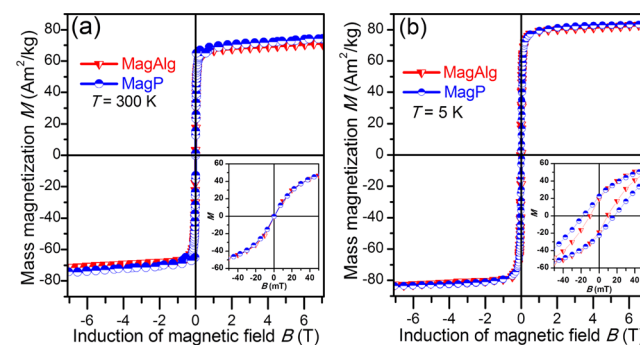


Figure 3. Hysteresis loops from MagP (blue circles) and MagAlg (red circles) recorded at the temperature of (a) 300 and (b) 5 K.

and Table 1). This is in full agreement with the XRD results, which indicated that MagAlg is formed by slightly smaller nanocrystallites, mirrored in the smaller coercive field.^{80,81} The measurements performed at 300 K confirmed the superparamagnetic nature for both systems and the very high M_s of 71.1 A m² kg⁻¹ with respect to the hybrid's mass. Despite the smaller nanocrystallite size of MagAlg, MagAlg, and MagP practically exhibited very similar M_s (~ 85.6 and 83.5 A m² kg⁻¹) with respect to the magnetic material content (Table 1, M_s Fe₂O₃). This observation can be rationalized upon examination of the high resolution TEM images discussed in the next section.

TEM Analysis. The TEM results of the colloidal nanoassemblies revealed the structural organization of the system, demonstrating that densely packed MIONs in MagAlg were arranged into superclusters (Figure 4a and Supporting

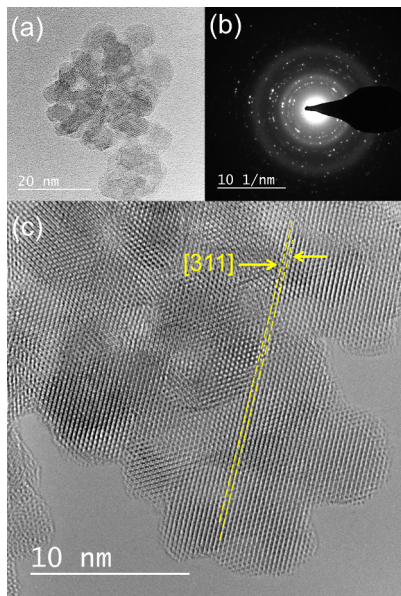


Figure 4. (a) TEM image of MagAlg. (b) SAED pattern. (c) HRTEM image of a selected area of the MagAlg cluster shown in (a) where the same crystal plane orientation becomes evident.

Information Figure Sa,b,c), unlike MagP.³⁵ The mean clusters' size was determined as ca. 40 nm, a value very close to the number-weighted D_h . From the high resolution TEM images (Figure 4c and Supporting Information Figure S4d,e) it became evident that large areas of the clustered material are built from crystallographically aligned nanocrystals. Nowadays, nonclassical crystal growth through epitaxial aggregation of preformed nanocrystallites toward mesoscale materials is a matter of high interest for the development of new materials with exciting properties.^{67,82–84} Nevertheless, it is for the first time that epitaxial co-CNCs of magnetite are developed through a soft biomimetic route at 50 °C under normal pressure, since until now epitaxial/oriented aggregation toward magnetite co-CNCs has been attained through solvothermal or high temperature thermolytic routes.

Although the same ferrous precursor has been previously used by our groups with different polymers during magnetite's arrested precipitation, only in this case, and using the reported synthetic conditions, alginate appeared to dictate the growing nanocrystallites toward controlled aggregation. It has been reported in the year 2000 in the *Science* journal that crystal growth of iron (hydroxy)oxide phases through biomimetic mineralization in bacteria can take place through epitaxial aggregation of smaller (2 nm) protocrystals, leading to crystallographically oriented but, otherwise, polycrystalline materials.⁸⁵ On the basis of their analysis, it was proposed that small protocrystallites initially approach each other and then may rotate and finally relax toward the energetically most favorable configuration. This dynamic process occurs only after the surface atoms find their lattice-matching atoms in the neighboring nanocrystallites. Here, we hypothesize that the present synthetic procedure, through a single ferrous precursor, which proceeds quite slowly toward the formation of magnetic phase (1 h and 30 min),⁸⁶ is

a critical factor that favored the oriented aggregation. This comes in immediate antithesis to the coprecipitation routes, a widely employed method that uses ferrous and ferric precursors. In the latter case addition of base to the mixture of $\text{Fe}^{2+,3+}$ produces in a subsecond time interval the black precipitate of magnetite. In the present case the reaction requires at least 30 min until the magnetic (black) phase develops through intermediate green iron hydroxide slurries. Thus, the slow crystallization rate might be crucial for the protocrystals to relax toward the energetically most favorable orientation.

From the observed magnetic trends, the question that emerges is how MagAlg and MagP can feature similar M_s values, despite of the fact that MagP is constituted by MIONs of larger diameter. Epitaxial aggregation in MagAlg may provide the explanation of this phenomenon, that is, the oriented crystal planes at the periphery of the primary MIONs in co-CNCs may result into suppression of structurally and magnetically disordered surface layers and thus to suppression of magnetization reduction phenomena, which are commonly encountered in MIONs and related materials.^{80,81} Similar reports for co-CNCs from the thermolytic route have also hypothesized that such behavior is the result of epitaxial aggregation and suppression of disordered surface layers.²⁵ Therefore, our observations for the biomimeticized co-CNCs and their comparison with the soft-CNCs (MagP) provide further and strong evidence supporting this rational.

Low Gradient Magnetophoresis. It has been envisioned that advances in mesocrystal synthesis might lead to advanced artificial materials.⁸⁷ In the present case, we bring into light for the first time that the condensed cluster superstructure has a distinctive advantage in comparison to soft-CNCs. In order to experimentally demonstrate this hypothesis we have used low gradient magnetophoresis, a technique that provides unique and complementary information to magnetometry when used carefully, i.e., when certain parameters are kept constant or appropriately adjusted in order to extract trustworthy conclusions. D_h , solvent viscosity, and nanocrystallite size are variables that should be kept constant when, for example, the aim is to probe the material's magnetization. Since in the present case it is important to investigate the superstructure within each colloidal nanoassembly, the M_s of the magnetic phase of the materials should be kept constant as well (see Figure 3 and Table 1). Finally, magnetic colloids of the same concentration had to be used, which displayed similar optical absorbance.

The magnetophoretic behavior of MagAlg was probed and compared to both MagP and the smaller sized MagAlg composed of 6 nm nanocrystallites prepared by coprecipitation which, as expected, displayed significantly lower M_s due to size effects.^{80,81} This sample, with $M_s(\text{Fe}_3\text{O}_4) = 35 \text{ A m}^2 \text{ kg}^{-1}$, is displayed as a measure for understanding that the difference in the slopes of the lines in Figure 5 between MagP (soft-CNC system) and MagAlg (co-CNC system) is very significant, if we consider that the difference between MagP and the 6 nm sample is the result of very high difference in M_s . It should be also noted here that magnetophoretic results of the studied samples recorded for different batches of the same product were identical, substantiating the credibility of the technique. Therefore, such a different behavior witnessed for MagAlg and MagP cannot be explained straightforwardly, since both systems have similar D_h and M_s . MagAlg clearly exhibits much higher magnetophoretic mobility. Therefore, the

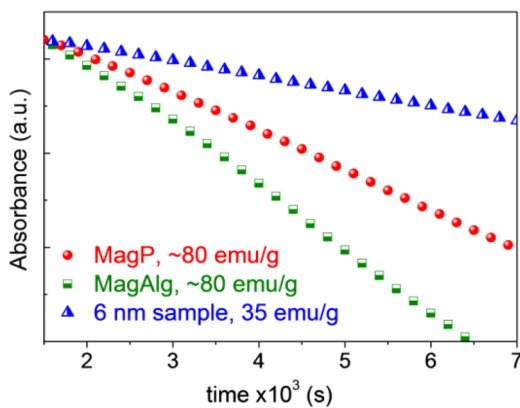


Figure 5. Magnetophoresis behavior of co-CNCs (MagAlg) and soft-CNCs (MagP), in comparison to the observed response of MagAlg formed by 6 nm nanocrystallites of $D_h \sim 100$ nm.

observed differences should be ascribed to the only difference left between these two samples, which is the morphological architecture of MagAlg.

We suggest that the epitaxially condensed-type superstructure allows for a larger amount of magnetic material to be caged in the core of the colloids, without increasing the hydrodynamic diameter, as opposed to the arrangement of soft-CNCs. On this basis, the high magnetophoretic mobility of MagAlg could be rationalized as follows. The velocity of a magnetic colloid being subject to a magnetic field gradient can be calculated using eq 1:⁸⁸

$$F_{\text{drag}} = 3\pi\eta D_h u \quad \text{and} \quad F_{\text{mag}} = (V_t M_s \nabla) B \quad (1)$$

When the colloid reaches a constant velocity, then $F_{\text{drag}} = F_{\text{mag}} \rightarrow u = (V_t M_s \nabla) B / 3\pi\eta D_h$, where F_{drag} is the drag force, η is the viscosity, u is the velocity, F_{mag} is the magnetic force, V_t is the total volume of magnetic material present in each colloidal entity, and B is the magnetic induction. Therefore, the velocity of the magnetic system is directly proportional to the volume of the magnetic material, which is present in each colloid, and inversely proportional to the hydrodynamic diameter of the colloid. Co-CNCs, such as MagAlg, may therefore represent the optimal structural organization able to maximize the V_t/D_h ratio.

At this point one would argue on how is it possible to have higher magnetic material content in each nanoassembly of co-CNCs (MagAlg), since it displays slightly lower inorganic content compared to MagP. Furthermore, based solely on the size of the clusters, the surface area in MagAlg should be smaller than MagP (in which MIONs are separated), and therefore a lower amount of polymer would be possible to reside on the MagAlg clusters' surface. Nevertheless, J. F. Banfield et al.⁸⁵ have identified that such naturally occurring epitaxial clusters have empty volume between nanocrystals of the same cluster, indicated by low contrast regions within the cluster, exactly as it occurs in the present case (Figure 4a and Supporting Information Figure S4a,b,c). In addition, there are several reports on artificial epitaxial magnetite co-CNCs, from thermolytic or solvothermal routes with significant porosity.^{15,23,62} Therefore, the surface area in MagAlg is not a limiting issue due to porosity presence. Finally, it is also known for other types of materials that oriented aggregation is occasionally promoted by polymeric coatings on the surface of the primary crystals.^{15,82,84} As a result, the possible presence of

polymer in between the MIONs of the cluster and in the space of the pores should not be excluded or come as a surprise.

Interactions of MagAlg with Doxorubicin. The suitability of MagAlg for applications in drug delivery was assessed by monitoring its drug loading and release attributes with the potent anticancer drug doxorubicin (Dox). MagAlg displayed very high loading ability for doxorubicin (26 wt % \pm 2), as shown in Figure 6a, at Dox/nanocarrier weight-feed ratio

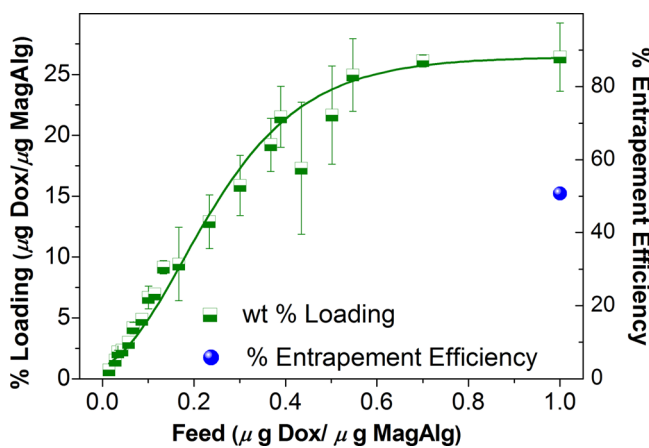


Figure 6. Doxorubicin loading profile (squares) in MagAlg and entrapment efficiency (circles).

of 0.5 to 0.6. The entrapment efficiency was also found very high, ranging from 60% to 80% (Figure 6a), and dropped down to 40% at higher feeds. Therefore, MagAlg worked flawlessly as a nanocarrier.

In our previous report on MagP³⁵ we have discussed and compared to other systems the magnetic and drug-loading properties of the nanocarrier. Comparisons with literature led to the conclusion that MagP was a unique material because it merged very effectively excellent M_s and high Dox loading. Nevertheless, MagAlg introduced further developments regarding doxorubicin loading and response to magnetic field.

For this reason, MagAlg provided the impetus for further evaluation. Drug release was monitored in phosphate buffered saline (pH = 7.4), and we found very low release and very slow release rate (Figure 7 a, blue circles); such behavior is vital for in vivo use, since it should grant to the nanoassemblies enough time to reach their target tissue/s before launching their cargo.

Modeling of the alginate–Dox complexes provided clear evidence for the strong intermolecular interactions, explaining the slow release rate. Multiple hydrogen bonding and electrostatic interactions result in strong binding of Dox in the alginate shell of the magnetic nanocrystallites (Figure 8). In addition, several H-bonding interactions between the two alginate chains are present which keep portions of its sugar monomers in close proximity to each other (Figure 8b, space-filling model). Such structural organization also suggests that an extended network of interchain interactions should be present in MagAlg and therefore may provide an additional explanation of the very desorption-resistant alginate shell, as previously discussed. Furthermore, it may prevent structural changes in the co-CNCs upon application of alternating magnetic fields (AMF) and temperature increase, as discussed in the next paragraph.

Lartigue et al.²⁵ found that clustering of MIONs enhances their ability to increase temperature during AMF. Thus, taking

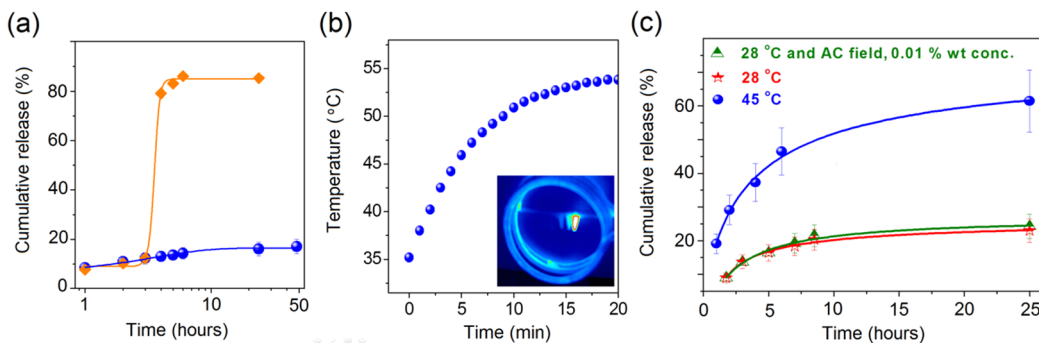


Figure 7. (a) Drug release kinetics with (rectangular orange data points) and without (round blue data points) the presence of AC magnetic field in PBS ($\text{pH} = 7.4$). (b) Temperature dependence as a function of the exposure time at AC field (400 kHz, 50 Oe (4 kA/m)). Inset: Infrared image of the magnetic nanocarriers recorded at the time of magnetic hyperthermia. (c) Dox release profiles under various environmental conditions.

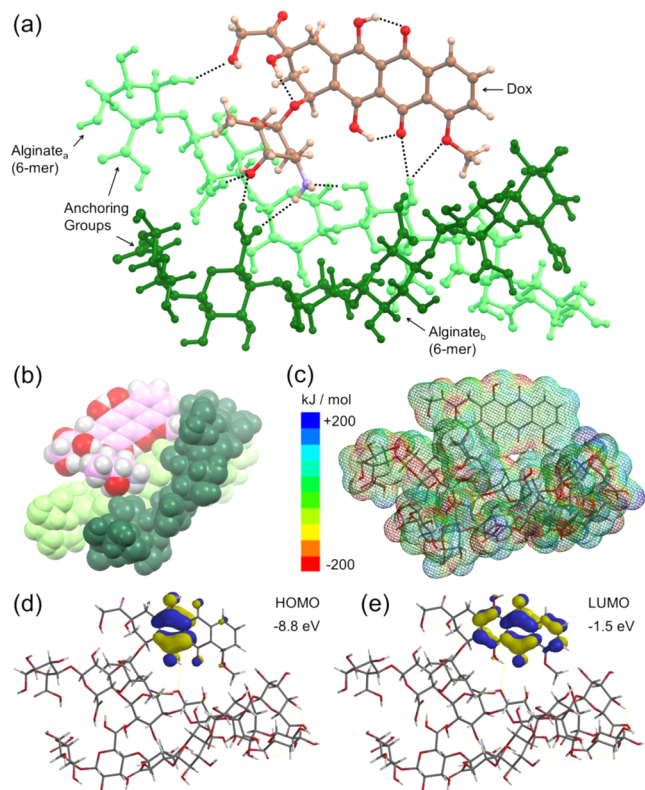


Figure 8. (a) The simplified MagAlg-Dox model, showing the through-space interaction of Dox and alginate chains in MagAlg. The broken lines highlight intra- and intermolecular H-bonding interactions between Dox and alginate. H-bonding interactions between the two alginate chains were not depicted for clarity. (b) Space-filling rendering of the MagAlg-Dox model and (c) electrostatic potential energy mapped surface calculated by RHF/RM1 (isoval 0.0023). (d, e) Frontier orbitals for MagAlg-Dox model (RHF/RM1, surfaces drawn at 0.032 isoval).

advantage of the magnetic properties of the co-CNCs, we tested the impact of AMF on triggering drug release.^{89,90} After three hours of normal release (Figure 7a), AMF was applied to a dispersion of drug-loaded nanocarriers (1% w/v in Fe_2O_3) and for a period of 30 min (Figure 7a, rectangular points), during which temperature increased above 55 °C, as evidenced from the control experiment of 1% w/v Fe_2O_3 in H_2O (Figure 7b). As shown in Figure 7a, the observed drug release kinetics changed profoundly and topped the remarkable value of ~90% release within the next hour. In order to elucidate the

mechanism of drug–release stimulation, we have performed release experiments (Figure 7c) at three different conditions: (i) 28 °C without AMF, (ii) 28 °C with AMF, and (iii) 45 °C without AMF. In these three experiments nanocarrier concentration was low: 0.01% w/v in Fe_2O_3 . At such low concentration there is no temperature increase during AMF, as well as no drug release stimulation, as shown in Figure 7c (green triangles). On the other hand, during experiments without AMF, at 45 °C significant release was observed (~60%), unlike the case of 28 °C. Therefore, results clearly show that release is triggered only in experiments where temperature rises, that is, only (a) at high nanocarrier concentration and AMF or (b) high temperature even without application of AMF. In conclusion, we demonstrated that the temperature and its ramifications (i.e., higher diffusion coefficient of doxorubicin and/or H-bonding weakening) are the cause for the increased release in the particular system. It should be stressed however that this mechanism is of course not universal. For instance, with the MagP system and cis-platin loading, the release of cis-platin takes place with AMF even when there is no temperature rise (data not yet published). There are reports in literature where triggered release has been attributed to temperature rise and not to mechanical vibration of MIONs.^{91,92} Others have identified mechanical motion and defect formation as important parameters as well.⁵⁹ Therefore, we may conclude for the time being that, depending on the studied system, different mechanisms for triggering release may apply each time. Further understanding of the physical origin underneath the witnessed strong binding of the Dox molecule to the MagAlg system can be obtained theoretically, and the details are discussed in the following section.

Theoretical Calculations. Binding of Dox to the organic-shell coating material (alginate) in MagAlg is thought to be driven by emergence of both hydrogen-bonding and electrostatic interactions. This effect can be tentatively rationalized by modeling theoretically the system. In order to reduce the otherwise large complexity associated with the structural organization of the condensed cluster MagAlg, we used for simplicity a model containing two alginate chains composed by alternating L-guluronate (G) and D-mannuronate (M) residues with small length (6-mer), placed in close proximity to each other and having on one side the carboxylate ($-\text{COOH}$) moieties constrained in fixed positions (6.65 Å, C–C through-space distance, labeled as anchoring groups in Figure 8a). These constrained carboxylates are thought to act as the active groups that bind the boundary surface iron of the magnetite cores. The conformational space of the system was sampled by

combination of the Monte Carlo algorithm (MC) coupled with Merck molecular mechanics force field (MMFF94aq), followed by geometry optimization of the best scored conformer using the Recife Model 1 (RM1) semiempirical method. The MC/MMFF94aq approach employed initially a simulated annealing of the system at high temperature (5000 K), followed by slow cooling to room temperature. The results from the conformational analyses (restricted search, 10 000 conformers considered, energy window of 40 kJ/mol) with MC/MMFF94aq clearly revealed that the group prone to be involved in H-bonding interactions with both the carboxylate and hydroxyl residues of the alginate chains was mostly the 4-amino-5-hydroxy-6-methyloxan residue of the Dox molecule in its chair conformation. On the contrary, the hydroxyl and methoxy residues located on the planar aromatic tetracyclic-5,12-dione moiety were statistically interacting more with the hydroxyl groups located on the alginate sugar backbones. Geometry optimization (RHF/RM1) of the best scored conformer led to a slight change in the geometry, which was accompanied by relaxation of the H-bonding distances (distances ranging from 1.8 Å to ~2.8 Å, Figure 8a, dotted lines) with respect to those obtained using Monte Carlo/MMFF94aq Merck force field (1.7–2.3 Å). In MagAlg-Dox, several H-bonding interactions between the two alginate chains are present, and those interactions keep portions of the sugar molecules in close proximity to each other (Figure 8b). Such structural organization strongly suggests that in the real MagAlg system an extended network of interchain interactions should be present, and, therefore, those interactions may prevent occurrence of large breathing effects in the condensed-cluster architecture in response to external AMF, in agreement with the experimental findings.

It is important to note that electrostatic interactions play also a vital role in the Dox binding and transport process. The planar aromatic chromophoric region of Dox interacts with the underneath alginate chains, as evidenced from the electrostatic potential energy surface (Figure 8c). Thus, it is likely that upon increasing the system temperature the conformational mobility of the alginate molecules might increase significantly, weakening both electrostatic and H-bonding interactions with the drug. Such effect should in turn favor drug diffusion and release into the bulk, as the experimental findings on this system suggested. Figure 8d illustrates the frontier orbitals obtained for the MagAlg-Dox model, evidencing that those molecular orbitals remained centered on the aromatic tetracyclic-5,12-dione moiety of Dox. More detailed comparison of the orbital distribution between Dox unbound and bound to alginate is provided in Supporting Information Figure S12.

Finally, it should be noted that in this model a third possible driving force for Dox loading has not been considered. It is about hydrophobic interactions between Dox molecules and the alginate shell. As Dox molecules bind to alginate, the hydrophilic groups of both Dox (amines) and alginate (carboxylates) are masked/screened due to the electrostatic interactions developed. Consequently, the shell becomes more and more hydrophobic, which in turn may drive more Dox molecules to reside inside the shell, due to hydrophobic interactions.

In Vitro and in Vivo Evaluation. The biological impact of the empty and Dox-loaded MagAlg was probed by MTT assay in terms of cell viability against human breast adenocarcinoma cell line (MCF7 cells, 24 h, 37 °C) in vitro. The bare MagAlg co-CNCs were tolerated very well, up to ~120 µg iron oxide/

mL (Figure 9a). This corresponds to ~50 µg Dox/mL (~92 µM Dox) when the drug-loaded MagAlg system is considered.

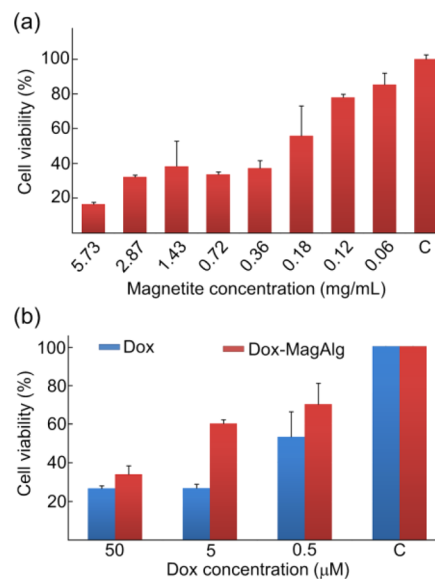


Figure 9. Cytotoxicity assays for (a) unloaded nanocarriers and (b) Dox-loaded nanocarriers compared to neat Dox.

Such high concentration of nanocarrier and, in turn, the amount of drug that can be transported in vivo is ~4–5 times greater than the recommended dose (60–75 mg per person/time, i.e., per 5 L of blood⁹³). Therefore, further discussion of the emergence of cytotoxicity becomes irrelevant when the nanocarrier concentration is higher than 120 µg/mL. We further screened the cytotoxic effect of free Dox and Dox-loaded MagAlg in MCF7 cells. The doses of the latter preparations were appropriately selected in order to perform tandem experiments using the same drug contents (amount of drug alone and amount of drug bound to MagAlg).

The results demonstrated that the cytotoxicity of Dox-loaded MagAlg consistently decreased in comparison to free doxorubicin, within the time window used in the experiment (24 h) (Figure 9b). Considering the very low release rate of Dox from the nanocarriers, these findings demonstrate that the MagAlg system, indeed, retains nicely the drug engulfed in vitro, and thus the Dox concentration released in the cells is lower than that witnessed for the free Dox. Such function is highly desirable for a drug delivery system, since it can grant to the nanocarriers enough time to reach the target and then it may release its payload aided by an external AMF (if high enough concentration of magnetic particles reach the target or are directly injected to the target) or by high temperature (i.e., tissue with inflammation).

The behavior of the Dox-loaded MagAlg is unique, in the sense that it is a rare literature example where drug loaded nanocarriers show less toxicity than the same amount of the free drug. For instance, other studies^{23,24,79} reported higher toxicity of drug-loaded co-CNCs than the actual free drug. This was attributed to the high endocytosis of the nanocarriers. On the contrary, the present Dox-loaded nanocarriers show reduced toxicity in comparison to the free drug which proves that the drug does not diffuse out of the nanocarriers at the normal environment of the cell medium, which strongly underpins the drug release studies.

MagAlg was *in vitro* evaluated as a negative contrast agent with a clinical MRI instrument. Its transverse relaxivity value of $r_2 = 243 \text{ mM}^{-1} \text{ Fe s}^{-1}$, as deduced from Figure 10, is particularly

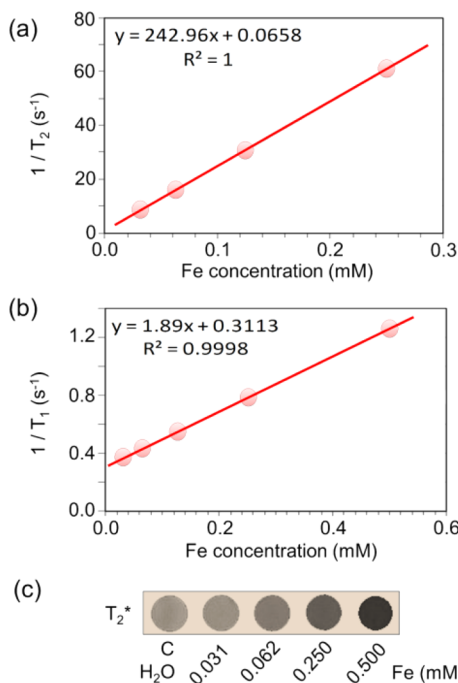


Figure 10. Transverse (a) and longitudinal (b) relaxation rates of the drug-free MagAlg nanocarriers, along with the linear regression fit. The agarose phantom experiment showing the T_2^* weighted images obtained versus increasing concentration of the MagAlg iron oxide nanoparticles (expressed in mM of Fe ions).

high for magnetic colloids of this size (i.e., $D_h = 45 \text{ nm}$ by number, see also Supporting Information Table S6). It is worth underlining that there are significant contributions in the literature that describe nanoparticulate magnetic systems with higher transverse relaxivities than MagAlg.^{27,34,37,40,41,43,44,54,55} However, in all of these instances the studied magnetic nanoassemblies display higher hydrodynamic size (Supporting Information Table S6). This value of relaxivity is practically the highest possible that can be attained for this size of magnetite CNCs. Pölselt et al.⁴³ experimentally found that clusters of volume- $D_h = \sim 65 \text{ nm}$ (the same with the present material) with primary nanocrystallites of 13 nm correspond indeed to $\sim 250 \text{ mM}^{-1} \text{ Fe s}^{-1}$. Only by further increasing D_h did r_2 values became higher (Figure 3f in the original paper).⁴³ Their results were also substantiated by theoretical calculations confirming that for 13 nm crystallites this is about the top relaxivity value that can be attained when cluster size is retained at this scale. Paquet et al.,⁴⁴ using a smart magnetic nanohydrogel colloid, have also reached similar conclusions: for number- $D_h = 50 \text{ nm}$, r_2 relaxivity was determined at $245 \text{ mM}^{-1} \text{ Fe s}^{-1}$ and increased only after further rise of the D_h . Very high r_2 of $700 \text{ mM}^{-1} \text{ Fe s}^{-1}$ has been attained by T.-J. Yoon et al. for 16 nm MIONs clustered in 86 nm (size by TEM, D_h not provided) colloids.⁵⁵

Unlike the previous examples, there are some instances where, although the D_h is only slightly higher, r_2 is significantly large. For example, (i) co-CNCs of number- $D_h = 60 \text{ nm}$, $r_2 = 540 \text{ mM}^{-1} \text{ Fe s}^{-1}$,²⁷ (ii) magnetoliposomes of number- $D_h = 55 \text{ nm}$, $r_2 = 1290 \text{ mM}^{-1} \text{ Fe s}^{-1}$ with MIONs of 6.5 nm ,⁵¹ (iii) MION-encapsulating polymer nanoparticles of number- $D_h = 65$

nm, $r_2 = 900 \text{ mM}^{-1} \text{ Fe s}^{-1}$,⁹⁴ and (iv) nanocubes of number- $D_h = 43 \text{ nm}$, $r_2 = 800 \text{ mM}^{-1} \text{ Fe s}^{-1}$.⁹⁵ These examples show that there are significant variations in recorded structure–property relationships (see Supporting Information Table S6 for a more complete list with bibliographic comparisons). One reason could be light scattering data interpretation. Quite often it is observed that large D_h values (intensity-based or z -average) are translated to very small volume or number-based D_h equivalents. Only when size polydispersity is low these values might not deviate much. For this reason it is necessary, in our opinion, that the complete light scattering data should be provided in order to extract more reliable conclusions. It has been also observed that relaxivity measurements might be subjective to variations depending on instrumentation and sample preparation. For instance it has been reported that r_2 estimation might vary upon the Fe ion concentration window where the measurement is performed^{39,47} or upon magnetic field strength.⁹⁶ Closing the MRI discussion, we wish to note that a very important aspect of the current material is that 83 wt % of MagAlg corresponds to magnetic material, imparting very high transverse relaxivity in terms of the hybrid's mass (not only Fe mass), which is, in our opinion, the true marker for the theranostic system's performance. The importance of the high content in magnetic material has been also underlined in the recent paper by P. Tartaj's group,⁹⁷ by stating in their introduction that high relaxivity of certain materials (i.e., $465 \text{ mM}^{-1} \text{ Fe s}^{-1}$) might not be accompanied by high magnetic material content and thus display very low M_s ($2 \text{ A m}^2 \text{ kg}^{-1}$).

MagAlg was finally investigated for its potential as dual imaging agent by utilizing Single Photon Emission Computed Tomography (SPECT), apart from MRI. Therefore, we first evaluated its proclivity to conjugate efficiently $^{99\text{m}}\text{Tc}$ using the direct radiolabeling method (see Experimental Section). MagP (the PEGylated system³⁵) was also subjected to the same testing.

The radiolabeled conjugates were found to be very stable in serum as indicated with ITLC (for indicative images see Supporting Information Figures S5 and S6). MagAlg retained up to 74% and MagP up to 63% of the radiolabel (see Table S3 in Supporting Information). Therefore, we proceeded to *in vivo* evaluation using scintigraphic imaging in normal mice. Sequential, whole body images provide noninvasively, several time points for MagP and MagAlg spatiotemporal biodistribution (Figure 11 a,b). MagAlg appeared to reside mostly in the liver, with local concentration over 60%, which was statistically significantly lower than the 80% observed for MagP. The lower concentration in liver indicates that MagAlg remains longer in blood circulation. More detailed biodistribution graphs are given in Supporting Information Figures S7, S8, and S9. It is quite surprising that the PEGylated system displays lower blood-circulation time. Even if PEG remains the gold standard in the field of nanomedicine it has some limitations such as its *in vivo* fate after systemic administration and the unreliable complement activation depending on the extent of PEGylation and on the molecule to which it is bound each time.⁹⁸ Such observations are conflicting in the literature and rely on the variable design and composition of nanoparticles, and these effects should be considered in each case separately.⁹⁹ In parallel to PEG, which only manages to delay the phagocytosis of nanoparticles as their destination to the reticulo endothelial system (RES) is unavoidable, coating of nanoparticles with polysaccharides has made great progress in relation to opsonin adsorption.¹⁰⁰ The present results confirm

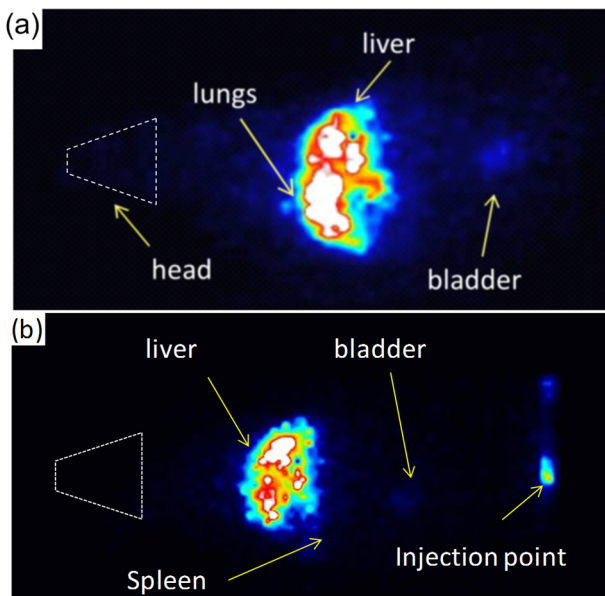


Figure 11. Scintigraphic images of (a) MagP and (b) MagAlg at 1 h post injection.

the potential of MagAlg to act as bimodal contrast agent and underline the diverse responses toward preferential localization in different organs, despite the fact that further functionalities have not yet been added in the organic corona.

CONCLUSIONS

The biominerization of functionalized colloidal nanocrystal clusters, grown through the epitaxial condensation (oriented aggregation) of primary magnetic iron oxide nanocrystallites, is described to take place under soft conditions: very low temperature and ambient pressure. It is also shown that condensed epitaxial clustering culminates to colloidal mesocrystals that may produce a far better response to manipulation by external magnetic fields than other types of clustered magnetic colloids (soft clusters), where magnetic nanocrystallites are not densely packed inside the colloidal nanoassembly. Biominerization in the presence of alginate is crucial for the crystallization process and facilitates the formation of functional corona. The latter ascribes to the products' high colloidal stability and excellent doxorubicin binding affinity as drug loading, release, and modeling studies indicate. These functions are attained only with 17 wt % polymer content, which in turn gives rise to very high saturation magnetization in comparison to current literature data. Finally, the system displays top sensitivity performance in medical diagnostics at the size of ~45 nm, due to both the large negative contrast in clinical MRI and for its ability for SPECT imaging, as it was shown with *in vivo* experiments.

Under this frame, MagAlg is currently under intensive studies toward its efficient derivatization with an outer biorepellent and protective canopy, in order to obtain a system encompassing higher circulation time *in vivo*.

ASSOCIATED CONTENT

Supporting Information

Mössbauer analysis and results. TGA results. Radiolabeling and biodistribution studies. Computational methods and results. Comparative table with literature data. This information is available free of charge via the Internet at <http://pubs.acs.org/>.

AUTHOR INFORMATION

Corresponding Author

(A.B.) E-mail: abakan@upatras.gr. Tel.: (+030) 2610969383.

Notes

The authors declare no competing financial interest.

ACKNOWLEDGMENTS

This research has been partly supported by the European Union and Greek national funds in the frame of Greece–Czech bilateral project (11CZ_026_EPAN2). The authors also acknowledge the contribution of the COST action TD1007 (<http://www.pet-mri.eu/index.html>), partial support by the Operational Program Research and Development for Innovations—European Regional Development Fund (CZ.1.05/2.1.00/03.0058), Operational Program Education for Competitiveness—European Social Fund (CZ.1.07/2.3.00/20.0017 and CZ.1.07/2.3.00/20.0058) of the Ministry of Education, Youth and Sports of the Czech Republic, and KONTAKT II research project (LH12085 of the Ministry of Education, Youth and Sports of the Czech Republic). We thank the Laboratory of Electron Microscopy and Microanalysis and the central XRD facility from Department of Geology of University of Patras, as well as the operators M. Kollia and P. Labropoulou. The TOC graphic was prepared by Mrs S. Stasinou.

ABBREVIATIONS

MIONs, magnetic iron oxide nanocrystallites; CNCs, colloidal nanocrystal clusters; co-CNCs, condensed-CNCs; Dox, doxorubicin; M_s , saturation magnetization; ITLC, instant thin layer chromatography; SPECT, single-photon emission computed tomography

REFERENCES

- (1) Koo, Y.-E. L.; Reddy, G. R.; Bhojani, M.; Schneider, R.; Philbert, M. A.; Rehemtulla, A.; Ross, B. D.; Kopelman, R. *Adv. Drug Delivery Rev.* **2006**, *58*, 1556.
- (2) Laurent, S.; Forge, D.; Port, M.; Roch, A.; Robic, C.; Vander Elst, L.; Muller, R. N. *Chem. Rev.* **2008**, *108*, 2064.
- (3) Colombo, M.; Carregal-Romero, S.; Casula, M. F.; Gutiérrez, L.; Morales, M. P.; Böhml, I. B.; Heverhagen, J. T.; Prosperi, D.; Parak, W. *J. Chem. Soc. Rev.* **2012**, *41*, 4306.
- (4) Ho, D.; Sun, X.; Sun, S. *Acc. Chem. Res.* **2011**, *44*, 875.
- (5) Ling, D.; Hyeon, T. *Small* **2013**, *9*, 1450. Mattheolabakis, G.; Rigas, B.; Constantinides, P. P. *Nanomedicine (London)* **2012**, *7*, 1577.
- (6) Jun, Y.-W.; Lee, J.-H.; Cheon, J. *Angew. Chem., Int. Ed.* **2008**, *47*, S122.
- (7) Perez, J. M.; Josephson, L.; O'Loughlin, T.; Högemann, D.; Weissleder, R. *Nat. Biotechnol.* **2002**, *20*, 816–820.
- (8) Min, C.; Shao, H.; Liang, M.; Yoon, T.-J.; Weissleder, R.; Lee, H. *ACS Nano* **2012**, *6*, 6821.
- (9) Sung Kim, K.; Park, J.-K. *Lab Chip* **2005**, *5*, 657.
- (10) Kokkinis, G.; Keplinger, F.; Giouroudi, I. *Biomicrofluidics* **2013**, *7*, 054117.
- (11) Galanzha, E. I.; Shashkov, E. V.; Kelly, T.; Kim, J.-W.; Yang, L.; Zharov, V. P. *Nat. Nanotechnol.* **2009**, *4*, 855.
- (12) Lee, J.-J.; Jeong, K. J.; Hashimoto, M.; Kwon, A. H.; Rwei, A.; Shankarappa, S. A.; Tsui, J. H.; Kohane, D. S. *Nano Lett.* **2013**, *13*, 1.
- (13) Chojnacki, P.; Mistlberger, G.; Klimant, I. *Angew. Chem., Int. Ed.* **2007**, *46*, 8850.
- (14) Deng, H.; Li, X.; Peng, Q.; Wang, X.; Chen, J.; Li, Y. *Angew. Chem., Int. Ed.* **2005**, *44*, 2782.
- (15) Zhu, Y.; Zhao, W.; Chen, H.; Shi, J. *J. Phys. Chem. C* **2007**, *111*, S281.
- (16) Ge, J.; Hu, Y.; Biasini, M.; Beyermann, W. P.; Yin, Y. *Angew. Chem. Int. Ed.* **2007**, *46*, 4420.

- (17) Barick, K. C.; Aslam, M.; Prasad, P. V.; Dravid, V. P.; Bahadur, D. *J. Magn. Magn. Mater.* **2009**, *321*, 1529.
- (18) Xuan, S.; Wang, Y.-X. J.; Yu, J. C.; Cham-Fai Leung, K. *Chem. Mater.* **2009**, *21*, 5079.
- (19) Xu, F.; Cheng, C.; Xu, F.; Zhang, C.; Xu, H.; Xie, X.; Yin, D.; Gu, H. *Nanotechnology* **2009**, *20*, 405102.
- (20) Hu, F.; MacRenaris, K. W.; Waters, E. A.; Schultz-Sikma, E. A.; Eckermann, A. L.; Meade, T. J. *Chem. Commun.* **2010**, *46*, 73.
- (21) Zhou, J.; Meng, L.; Feng, X.; Zhang, X.; Lu, Q. *Angew. Chem., Int. Ed.* **2010**, *49*, 8476.
- (22) Luo, B.; Song, X.-J.; Zhang, F.; Xia, A.; Yang, W.-L.; Hu, J.-H.; Wang, C.-C. *Langmuir* **2010**, *26*, 1674.
- (23) Luo, B.; Xu, S.; Luo, A.; Wang, W.-R.; Wang, S.-L.; Guo, J.; Lin, Y.; Zhao, D.-Y.; Wang, C.-C. *ACS Nano* **2011**, *5*, 1428.
- (24) Xing, R.; Wang, X.; Zhang, C.; Wang, J.; Zhang, Y.; Song, Y.; Guo, Z. *J. Mater. Chem.* **2011**, *21*, 11142.
- (25) Lartigue, L.; Hugounenq, P.; Alloyeau, D.; Clarke, S. P.; Lévy, M.; Bacri, J.-C.; Bazzi, R.; Brougham, D. F.; Wilhelm, C.; Gazeau, F. *ACS Nano* **2012**, *6*, 10935.
- (26) Xu, S.; Luo, Z.; Han, Y.; Guo, J.; Wang, C. *RSC Adv.* **2012**, *2*, 2739.
- (27) Xu, F.; Cheng, C.; Chen, D.-X.; Gu, H. *ChemPhysChem* **2012**, *13*, 336.
- (28) Xu, S.; Sun, C.; Guo, J.; Xu, K.; Wang, C. *J. Mater. Chem.* **2012**, *22*, 19067.
- (29) Ditsch, A.; Laibinis, P. E.; Wang, D. I. C.; Hatton, T. A. *Langmuir* **2005**, *21*, 6006.
- (30) Lee, J.-H.; Jun, Y.; Yeon, S.-I.; Shin, J.-S.; Cheon, J. *Angew. Chem., Int. Ed.* **2006**, *45*, 8160.
- (31) Sondjaja, R.; Hatton, T. A.; Tam, M. K. C. *J. Magn. Magn. Mater.* **2009**, *321*, 2393.
- (32) Berret, J.-F.; Schonbeck, N.; Gazeau, F.; El Kharrat, D.; Sandre, O.; Vacher, A.; Airiau, M. *J. Am. Chem. Soc.* **2006**, *128*, 1755.
- (33) Zhang, Q.; Thompson, M. S.; Carmichael-Baranauskas, A. Y.; Caba, B. L.; Zalich, M. A.; Lin, Y.-N.; Mefford, O. T.; Davis, R. M.; Riffle, J. S. *Langmuir* **2007**, *23*, 6927.
- (34) Pothayee, N.; Balasubramaniam, S.; Pothayee, N.; Jain, N.; Hu, N.; Lin, Y.; Davis, R. M.; Sriranganathan, N.; Koretsky, A. P.; Riffle, J. S. *J. Mater. Chem. B* **2013**, *1*, 1142.
- (35) Bakandritsos, A.; Papagiannopoulos, A.; Anagnostou, E. N.; Avgoustakis, K.; Zboril, R.; Pispas, S.; Tucek, J.; Ryukhtin, V.; Bouropoulos, N.; Kolokithas-Ntoukas, A.; Steriotis, T. A.; Keiderling, U.; Winnefeld, F. *Small* **2012**, *8*, 2381.
- (36) Xu, H.; Cui, L.; Tong, N.; Gu, H. *J. Am. Chem. Soc.* **2006**, *128*, 15582.
- (37) Ai, H.; Flask, C.; Weinberg, B.; Shuai, X. -T.; Pagel, M. D.; Farrell, D.; Duerk, J.; Gao, J. *Adv. Mater.* **2005**, *17*, 1949.
- (38) Kim, J.; Lee, J. E.; Lee, S. H.; Yu, J. H.; Lee, J. H.; Park, T. G.; Hyeon, T. *Adv. Mater.* **2008**, *20*, 478.
- (39) Talelli, M.; Rijcken, C. J. F.; Lammers, T.; Seevinck, P. R.; Storm, G.; van Nostrum, C. F.; Hennink, W. E. *Langmuir* **2009**, *25*, 2060.
- (40) Yang, J.; Lee, C.-H.; Ko, H.-J.; Suh, J.-S.; Yoon, H.-G.; Lee, K.; Huh, Y.-M.; Haam, S. *Angew. Chem., Int. Ed.* **2007**, *46*, 8836–8839.
- (41) Lim, E.-K.; Jang, E.; Kim, B.; Choi, J.; Lee, K.; Suh, J.-S.; Huh, Y.-M.; Haam, S. *J. Mater. Chem.* **2011**, *21*, 12473.
- (42) Bakandritsos, A.; Mattheolabakis, G.; Zboril, R.; Bouropoulos, N.; Tucek, J.; Fatouros, D. G.; Avgoustakis, K. *Nanoscale* **2010**, *2*, 564.
- (43) Pösel, E.; Kloust, H.; Tromsdorf, U.; Janschel, M.; Hahn, C.; Maßlo, C.; Weller, H. *ACS Nano* **2012**, *6*, 1619.
- (44) Paquet, C.; de Haan, H. W.; Leek, D. M.; Lin, H.-Y.; Xiang, B.; Tian, G.; Kell, A.; Simard, B. *ACS Nano* **2011**, *5*, 3104.
- (45) Hickey, R. J.; Haynes, A. S.; Kikkawa, J. M.; Park, S.-J. *J. Am. Chem. Soc.* **2011**, *133*, 1517.
- (46) Sanson, C.; Diou, O.; Thévenot, J.; Ibarboure, E.; Soum, A.; Brûlet, A.; Miraux, S.; Thiaudière, E.; Tan, S.; Brisson, A.; Dupuis, V.; Sandre, O.; Lecommandoux, S. *ACS Nano* **2011**, *5*, 1122.
- (47) Bigall, N. C.; Wilhelm, C.; Beoutis, M.-L.; García-Hernandez, M.; Khan, A. A.; Giannini, C.; Sánchez-Ferrer, A.; Mezzenga, R.; Materia, M. E.; Garcia, M. A.; et al. *Chem. Mater.* **2013**, *25*, 1055.
- (48) Béalle, G.; Di Corato, R.; Kolosnjaj-Tabi, J.; Dupuis, V.; Clément, O.; Gazeau, F.; Wilhelm, C.; Ménager, C. *Langmuir* **2012**, *28*, 11834.
- (49) Meledandri, C. J.; Ninjabgar, T.; Brougham, D. F. *J. Mater. Chem.* **2011**, *21*, 214.
- (50) Martina, M.-S.; Fortin, J.-P.; Ménager, C.; Clément, O.; Barratt, G.; Grabielle-Madelmont, C.; Gazeau, F.; Cabuil, V.; Lesieur, S. *J. Am. Chem. Soc.* **2005**, *127*, 10676.
- (51) Mikhaylov, G.; Mikac, U.; Magaeva, A. A.; Itin, V. I.; Naiden, E. P.; Psakhye, I.; Babes, L.; Reinheckel, T.; Peters, C.; Zeiser, R.; Bogyo, M.; Turk, V.; Psakhye, S. G.; Turk, B.; Vasiljeva, O. *Nat. Nanotechnol.* **2011**, *6*, 594.
- (52) Skouras, A.; Mourtas, S.; Markoutsas, E.; De Goltstein, M.-C.; Wallon, C.; Catoen, S.; Antimisiaris, S. G. *Nanomedicine Nanotechnol. Biol. Med.* **2011**, *7*, 572–579.
- (53) Qiu, P.; Jensen, C.; Charity, N.; Towner, R.; Mao, C. *J. Am. Chem. Soc.* **2010**, *132*, 17724–17732.
- (54) Taboada, E.; Solanas, R.; Rodríguez, E.; Weissleder, R.; Roig, A. *Adv. Funct. Mater.* **2009**, *19*, 2319–2324.
- (55) Yoon, T.-J.; Lee, H.; Shao, H.; Hilderbrand, S. A.; Weissleder, R. *Adv. Mater.* **2011**, *23*, 4793.
- (56) Lin, Y.-S.; Abadeer, N.; Hurley, K. R.; Haynes, C. L. *J. Am. Chem. Soc.* **2011**, *133*, 20444.
- (57) Peiris, P. M.; Toy, R.; Doolittle, E.; Pansky, J.; Abramowski, A.; Tam, M.; Vicente, P.; Tran, E.; Hayden, E.; Camann, A.; Mayer, A.; Erokwu, B. O.; Berman, Z.; Wilson, D.; Baskaran, H.; Flask, C. A.; Keri, R. A.; Karathanasis, E. *ACS Nano* **2012**, *6*, 8783.
- (58) Park, J.-H.; von Maltzahn, G.; Zhang, L.; Schwartz, M. P.; Ruosahti, E.; Bhatia, S. N.; Sailor, M. J. *Adv. Mater.* **2008**, *20*, 1630.
- (59) Peiris, P. M.; Bauer, L.; Toy, R.; Tran, E.; Pansky, J.; Doolittle, E.; Schmidt, E.; Hayden, E.; Mayer, A.; Keri, R. A.; Griswold, M. A.; Karathanasis, E. *ACS Nano* **2012**, *6*, 4157.
- (60) Lu, Z.; Yin, Y. *Chem. Soc. Rev.* **2012**, *41*, 6874–6887.
- (61) Guo, J.; Yang, W.; Wang, C. *Adv. Mater.* **2013**, *25*, 5196.
- (62) Li, D.; Tang, J.; Wei, C.; Guo, J.; Wang, S.; Chaudhary, D.; Wang, C. *Small* **2012**, *8*, 2690.
- (63) Wang, C.; Xu, H.; Liang, C.; Liu, Y.; Li, Z.; Yang, G.; Cheng, L.; Li, Y.; Liu, Z. *ACS Nano* **2013**, *7*, 6782.
- (64) Dames, P.; Gleich, B.; Flemmer, A.; Hajek, K.; Seidl, N.; Wieckhorst, F.; Eberbeck, D.; Bittmann, I.; Bergemann, C.; Weyh, T.; Trahms, L.; Rosenecker, J.; Rudolph, C. *Nat. Nanotechnol.* **2007**, *2*, 495.
- (65) Barick, K. C.; Aslam, M.; Lin, Y.-P.; Bahadur, D.; Prasad, P. V.; Dravid, V. P. *J. Mater. Chem.* **2009**, *19*, 7023.
- (66) Liu, J.; Sun, Z.; Deng, Y.; Zou, Y.; Li, C.; Guo, X.; Xiong, L.; Gao, Y.; Li, F.; Zhao, D. *Angew. Chem., Int. Ed.* **2009**, *48*, 5875.
- (67) Yuwono, V. M.; Burrows, N. D.; Soltis, J. A.; Penn, R. L. *J. Am. Chem. Soc.* **2010**, *132*, 2163.
- (68) Prochazka, R.; Tucek, P.; Tucek, J.; Marek, J.; Mashlan, M.; Pechousek, J. *Meas. Sci. Technol.* **2010**, *21*, 025107.
- (69) Torres Martin de Rosales, R.; Tavaré, R.; Glaria, A.; Varma, G.; Protti, A.; Blower, P. J. *Bioconjugate Chem.* **2011**, *22*, 455.
- (70) Bakandritsos, A.; Mattheolabakis, G.; Chatzikyriakos, G.; Szabo, T.; Tzitzios, V.; Kouzoudis, D.; Couris, S.; Avgoustakis, K. *Adv. Funct. Mater.* **2011**, *21*, 1465.
- (71) Ma, H.; Qi, X.; Maitani, Y.; Nagai, T. *Int. J. Pharm.* **2007**, *333*, 177.
- (72) Xu, X. Q.; Shen, H.; Xu, J. R.; Xie, M. Q.; Li, X. *J. Appl. Surf. Sci.* **2006**, *253*, 2158.
- (73) Petros, R. A.; DeSimone, J. M. *Nat. Rev. Drug Discovery* **2010**, *9*, 615.
- (74) Torchilin, V. P. Passive and Active Drug Targeting: Drug Delivery to Tumors as an Example. In *Drug Delivery*; Schäfer-Korting, M., Ed.; Handbook of Experimental Pharmacology; Springer: Berlin, Heidelberg, 2010; pp 3–53.

- (75) Bakandritsos, A.; Psarras, G. C.; Boukos, N. *Langmuir* **2008**, *24*, 11489.
- (76) Tóth, I. Y.; Illés, E.; Bauer, R. A.; Nesztor, D.; Szekeres, M.; Zupkó, I.; Tombácz, E. *Langmuir* **2012**, *28*, 16638.
- (77) Hagan, S. A.; Coombes, A. G. A.; Garnett, M. C.; Dunn, S. E.; Davies, M. C.; Illum, L.; Davis, S. S.; Harding, S. E.; Purkiss, S.; Gellert, P. R. *Langmuir* **1996**, *12*, 2153.
- (78) Yang, L.; Alexandridis, P. *Curr. Opin. Colloid Interface Sci.* **2000**, *5*, 132.
- (79) Ma, W.-F.; Wu, K.-Y.; Tang, J.; Li, D.; Wei, C.; Guo, J.; Wang, S.-L.; Wang, C.-C. *J. Mater. Chem.* **2012**, *22*, 15206.
- (80) Leslie-Pelecky, D. L.; Rieke, R. D. *Chem. Mater.* **1996**, *8*, 1770.
- (81) Jun, Y.; Seo, J.; Cheon, J. *Acc. Chem. Res.* **2008**, *41*, 179.
- (82) Cölfen, H.; Mann, S. *Angew. Chem., Int. Ed.* **2003**, *42*, 2350.
- (83) Cölfen, H.; Antonietti, M. *Angew. Chem., Int. Ed.* **2005**, *44*, 5576.
- (84) Niederberger, M.; Cölfen, H. *Phys. Chem. Chem. Phys.* **2006**, *8*, 3271.
- (85) Banfield, J. F.; Welch, S. A.; Zhang, H.; Ebert, T. T.; Penn, R. L. *Science* **2000**, *289*, 751.
- (86) Bakandritsos, A.; Bouropoulos, N.; Zboril, R.; Iliopoulos, K.; Boukos, N.; Chatzikyriakos, G.; Couris, S. *Adv. Funct. Mater.* **2008**, *18*, 1694.
- (87) Alivisatos, A. P. *Science* **2000**, *289*, 736.
- (88) Lim, J.; Lanni, C.; Evarts, E. R.; Lanni, F.; Tilton, R. D.; Majetich, S. A. *ACS Nano* **2011**, *5*, 217.
- (89) Kumar, C. S. S. R.; Mohammad, F. *Adv. Drug Delivery Rev.* **2011**, *63*, 789.
- (90) Riedinger, A.; Guardia, P.; Curcio, A.; Garcia, M. A.; Cingolani, R.; Manna, L.; Pellegrino, T. *Nano Lett.* **2013**, *13*, 2399.
- (91) Amstad, E.; Kohlbrecher, J.; Müller, E.; Schweizer, T.; Textor, M.; Reimhult, E. *Nano Lett.* **2011**, *11*, 1664.
- (92) Derfus, A. M.; von Maltzahn, G.; Harris, T. J.; Duza, T.; Vecchio, K. S.; Ruoslahti, E.; Bhatia, S. N. *Adv. Mater.* **2007**, *19*, 3932.
- (93) Erttmann, R.; Erb, N.; Steinhoff, A.; Landbeck, G. *J. Cancer Res. Clin. Oncol.* **1988**, *114*, 509.
- (94) Moffat, B. A.; Reddy, G. R.; McConville, P.; Hall, D. E.; Chenevert, T. L.; Kopelman, R. R.; Philbert, M.; Weissleder, R.; Rehemtulla, A.; Ross, B. D. *Mol. Imaging* **2003**, *2*, 324.
- (95) Lee, N.; Choi, Y.; Lee, Y.; Park, M.; Moon, W. K.; Choi, S. H.; Hyeon, T. *Nano Lett.* **2012**, *12*, 3127.
- (96) Martin Rohrer, H. B. *Invest. Radiol.* **2005**, *40*, 715.
- (97) Rebollodo, A. F.; Laurent, S.; Calero, M.; Villanueva, A.; Knobel, M.; Marco, J. F.; Tartaj, P. *ACS Nano* **2010**, *4*, 2095.
- (98) Knop, K.; Hoogenboom, R.; Fischer, D.; Schubert, U. S. *Angew. Chem., Int. Ed.* **2010**, *49*, 6288.
- (99) Kamaly, N.; Xiao, Z.; Valencia, P. M.; Radovic-Moreno, A. F.; Farokhzad, O. C. *Chem. Soc. Rev.* **2012**, *41*, 2971.
- (100) Lemarchand, C.; Grefa, R.; Couvreur, P. *Eur. J. Pharm. Biopharm.* **2004**, *58*, 327.